

Kaibao Wang and Liu Yang*

Investigation of fibre-modified silica aerogel composites

<https://doi.org/10.1515/ijmr-2023-0201>

Received June 20, 2023; accepted April 5, 2024;

published online August 16, 2024

Abstract: This investigation evaluates the thermal and mechanical performance of fibre-reinforced silica aerogel composites by introducing an optimised fabrication process and vacuumization. The novelty of this investigation was the identification of the minimum amount of solvent being used to synthesise aerogel, as well as the introduction of temperature ageing (45 °C). These provide a valuable guide for lowering the fabricating cost with optimised properties of aerogel composites. The glass fibre (GF)–aerogel composites obtained from the optimised process showed excellent thermal conductivity ($18.4 \text{ mW m}^{-1} \text{ K}^{-1}$ at a pressure load of 2 psi (13.8 kPa)). It is worth mentioning that vacuum sealing of the aerogel composites not only prevents dustiness during handling but also improves the thermal performance. The thermal conductivity could be further reduced to $13.8 \text{ mW m}^{-1} \text{ K}^{-1}$ by vacuum sealing the GF–aerogel composite. The compression and bending tests proved that the aerogel composites could endure considerable compressive and flexural strain without structural destruction. These outstanding characteristics indicate that GF–aerogel composites have great potential in the thermal insulation field, especially for a moderate temperature environment (i.e., less than 800 °C).

Keywords: silica aerogel; glass fibre; superior thermal conductivity; vacuum-sealed blanket; pressure load

1 Introduction

Aerogel is a type of solid material with a highly porous structure, a chain or pearl string shape three-dimensional network.¹ It has unique properties such as high specific

surface area ($500\text{--}1,500 \text{ m}^2 \text{ g}^{-1}$), high porosity (80–99 %), low bulk density ($0.03\text{--}0.35 \text{ g cm}^{-3}$), low thermal conductivity ($12\text{--}30 \text{ mW m}^{-1} \text{ K}^{-1}$), high acoustic resistance and strong adsorption.^{1,2} Aerogel can, therefore, be widely used in many fields, such as aerospace, building insulation, catalytic adsorption, and biomedicine.¹ However, this unique structure possesses fragile and low mechanical property characteristics, limiting development and application.

Silica aerogel is synthesised through sol-gel chemistry, defined by IUPAC as ‘the process through which a network is formed from solution by a progressive change of liquid precursors into a sol, to a gel, and in most cases finally to a dry network’.^{1,3} The parameters at each stage could have a significant impact on the final properties of aerogel, and these have been investigated extensively. Neugebauer et al. developed a technique for compacting a bed of granular silica aerogel, which concluded that compaction of the granules could significantly affect the thermal conductivity of aerogel granules.⁴ Li et al. reviewed the conventional and emerging synthesis and characterisation methods of silica aerogel in recent years, followed by a discussion on thermophysical properties. The reviews highlighted the possible solutions for the successful translation and industry uptake and focused on the emerging applications in electric vehicles and building insulation.⁵ In terms of the drying process, ambient pressure drying has then been widely used to synthesise silica aerogel due to the economic benefits. Collapse and shrinkage of the pores are the main challenges via ambient pressure drying. The embedment of fibres in silica aerogel could, to a large extent, prevent or minimise shrinkage during drying.¹

Fibre as a reinforcement is widely adopted to improve the pore structure and mechanical properties of composites. Fibres can be specified as organic and inorganic, depending on their chemical composition. Inorganic fibres such as glass fibres,^{6,7} ceramic fibres,⁸ carbon fibres,⁹ and mullite fibres,¹⁰ have been reported to manufacture fibre-reinforced aerogel composites. The organic fibres mainly include cotton fibres,¹¹ aramid fibres¹² and PET fibres.^{13,14} Huang et al. developed a novel fabrication process for the manufacture of glass fibre-reinforced silica aerogel composites, where the entire preparation period can be as short as 20 h. The obtained aerogel composites showed an excellent flexural modulus of elasticity of 12 MPa and thermal conductivity of

*Corresponding author: Liu Yang, Department of Mechanical and Aerospace Engineering, University of Strathclyde, 75 Montrose Street, Glasgow, G1 1XT, UK, E-mail: l.yang@strath.ac.uk. <https://orcid.org/0000-0001-8475-1757>

Kaibao Wang, Department of Mechanical and Aerospace Engineering, University of Strathclyde, Glasgow, G1 1XJ, UK. <https://orcid.org/0000-0002-1547-4677>

26 mW m⁻¹ K⁻¹.⁷ Lyu et al. conducted compression testing of ceramic fibre-reinforced silica aerogel composites at room temperature and elevated temperature (300 °C, 600 °C and 900 °C) to investigate aerogel composites' mechanical behaviour in a high-temperature environment. The results indicated that the compressive strength and modulus both increased with increasing exposure temperature, but the deformation recovery capability decreased.⁸ Preparation of SiO₂ aerogel with fibre as reinforcement phase improves the mechanical properties of aerogel to some extent, but the defects inherent in the reinforcement phase are also brought into the SiO₂ aerogel. For example, the fibres could increase the thermal conductivity of the composite. At the same time, using fibre as the reinforcement phase, no chemical bond is formed between the reinforcing body and the aerogel, which does not fundamentally improve the fragile defect of the SiO₂ aerogel. As the number of times of usage increases, aerogel could peel off from fibre, and the phenomenon of dust and powder falling would potentially be presented.¹⁵

The challenge to manufacture fibre-reinforced aerogel composites is to preserve the insulation properties, minimise the increase of apparent density, and improve the dustiness due to the weak interfacial bonding between the aerogel particle and fibres.¹ 'Vacuumization' can further improve the insulation performance and the service life of aerogel composites. The vacuum insulation board with aerogel composites as the core material can effectively minimise the heat transfer via air convection, which significantly reduces its thermal conductivity.¹⁶ It was suggested that the evacuation and sealing of silica aerogels could reduce the thermal conductivity by 50%.¹⁷ More importantly, the sealing of aerogel composites can prevent dust release during handling and processing. The International Energy Agency has conducted an energy in buildings and communities programme which investigated the long-term performance of super-insulating materials in building components and systems. Vacuum insulated panels (VIP) and aerogel were mainly investigated, proving the excellent thermal performance for the application of utilising these super insulating materials in building.^{18,19}

In this work, glass fibre mats were embedded in silica sol to form fibre-reinforced aerogel composites. The fabrication process, including the ageing temperature and drying process, was optimised to improve the physical, thermal and mechanical properties of the aerogel composite. The prepared aerogel composite was then vacuum sealed to prevent dustiness during handling, and its influence on thermal conductivity was investigated. The novelty of this

investigation was the identification of the minimum amount of solvent being used to synthesise aerogel, as well as the introduction of temperature ageing (45 °C). These provide a useful guide for lowering the fabricating cost with optimised properties of aerogel composites.

2 Experimental

2.1 Materials

The precursor used to synthesise aerogel was sodium silicate (34.6 wt.%, VWR UK, Na₂O:SiO₂ ≈ 3.43). Other agents, including hydrochloric acid (HCl, 37%), ammonia solution (NH₄OH, 28%), ethanol (EtOH), n-Hexane (95%) and chlorotrimethylsilane (TMCS ≥ 98% GC), were purchased from VWR UK. The polyethylene terephthalate (PET) fibre-needled blanket (AIRBLEED 10) was supplied by Aerovac systems Keighley Ltd. The density of the material is 55 kg m⁻³ with a nominal thickness of 6 mm without compression. The glass fibre needled mat was purchased from an online store (Mijexhaust Ltd.); the density of the fibre mat was 120 kg m⁻³ with a thickness of 10 mm.

2.2 Sample preparation

2.2.1 The fabrication process of aerogel blanket

Figure 1 is a schematic diagram for the preparation of silica aerogel and fibre-reinforced aerogel composites. Sodium silicate was diluted with deionised water with a 1:3 vol ratio. Hydrolysis of the diluted sodium silicate solution was carried out by adding 6 M HCl while stirring, forming silicic acid sol with a *pH* of ~2.0. The hydrogel was prepared by adding 2 M while stirring to reach a *pH* of ~5.0. The silica sol was poured into the PET blanket or GF mat in a mould. The mat was impregnated in the sol for 4 min. The excessive silica sol was then poured out, and the quantity was measured using a beaker. The amount of silica sol attached to fibres was calculated by subtracting the amount of sol poured out from the total volume (the volume of sodium silicate, HCl and NH₄OH). Gelation occurred within 30 min, and a porous network was formed. EtOH was used for ageing with a 2:1 vol ratio to the gel (the amount of sol attached to fibres). It was experimentally demonstrated that there was a minimum solvent-to-gel ratio (2:1) to fabricate aerogel successfully. When the amount of solvent was less efficient (i.e., 1:1 and 1.5:1), the water inside the gel may not be replaced by the

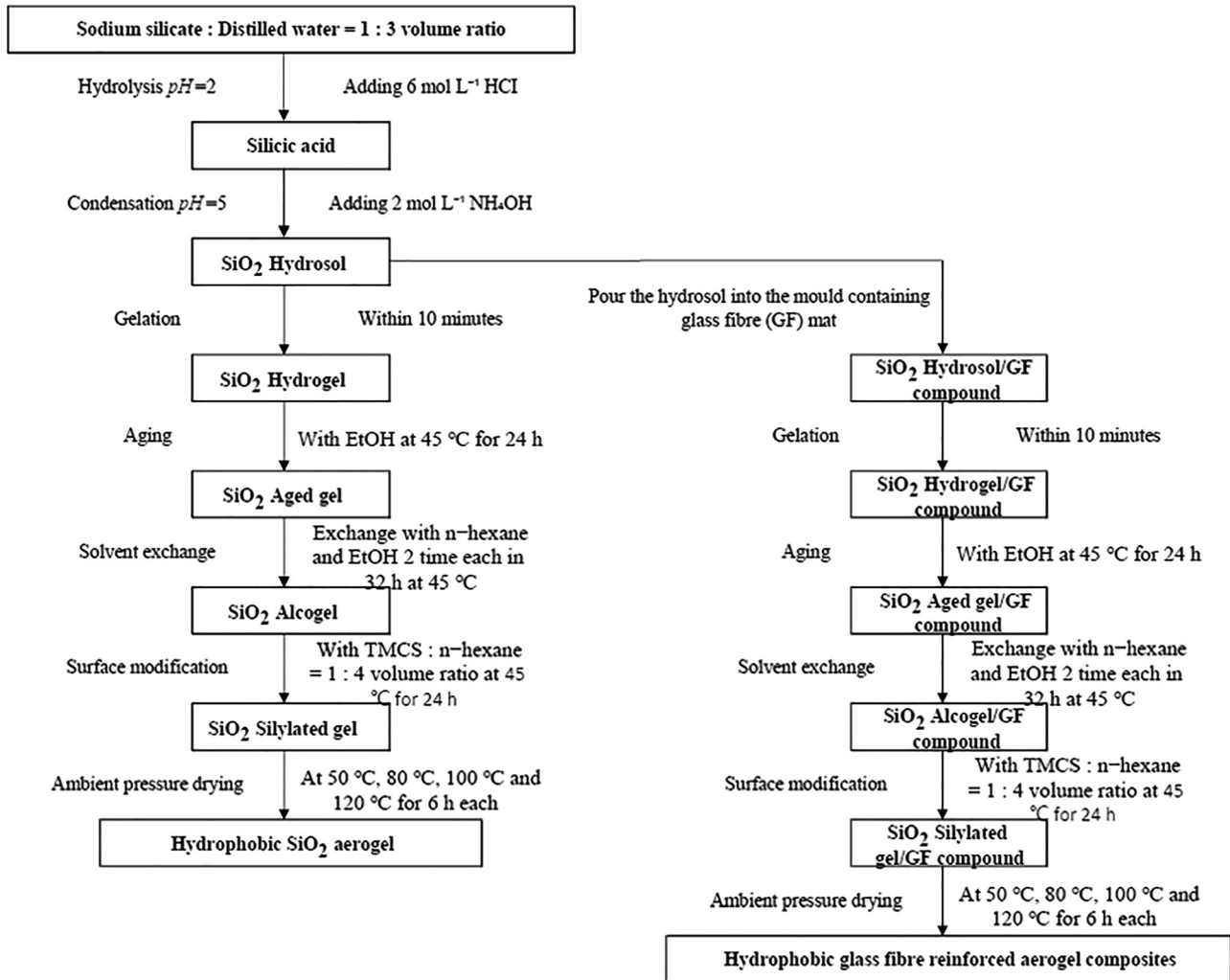


Figure 1: Schematic diagram for the preparation of silica aerogel and fibre-reinforced aerogel composites.

solvent completely. As a result, large capillary pressure was presented due to the high surface tension of water. Thus, powder form or small piece was fabricated after the drying process.²⁰ The ageing process was conducted at 45 °C for 24 h. EtOH was replaced by n-Hexane twice in 32 h at 45 °C. The surface modification was carried out by adding the silylating mixture of TMCS: n-Hexane with a volume ratio of 1:4 for 24 h at 45 °C. It was indicated that the aerogel aged and solvent-exchanged at a higher temperature (45 °C) led to a lower apparent density, higher specific surface area and pore volume, and finer average pore diameter. Ageing and solvent-exchanging at a higher temperature might also have enhanced the backbone strength and reduced the collapse or cracking of silica aerogel during the drying process.²⁰ Finally, the silylated gel was dried in ambient pressure at 50 °C, 80 °C, 100 °C, and 120 °C for 6 h, respectively, to obtain hydrophobic PET or GF-silica aerogel composites. The

fabrication process of the GF-aerogel composite is shown in Figure 2.

2.2.2 Vacuum sealing of aerogel blanket

It was stated that the thermal conductivity of aerogel composites could be reduced by vacuuming and sealing the blanket.¹⁷ In addition, the sealing of aerogel composites could prevent dust release during handling and processing. It was decided to investigate the benefits of vacuum sealing of the aerogel blankets.

The aerogel composite was placed in a vacuum-sealing bag, and the open end of the bag was sealed using a commercial food sealer. A vacuum pump was then used to evacuate the air by inserting a needle into the sealing bag. The vacuum pressure was controlled below -0.8 bar. The needle hole was finally melted using a hair straightener.

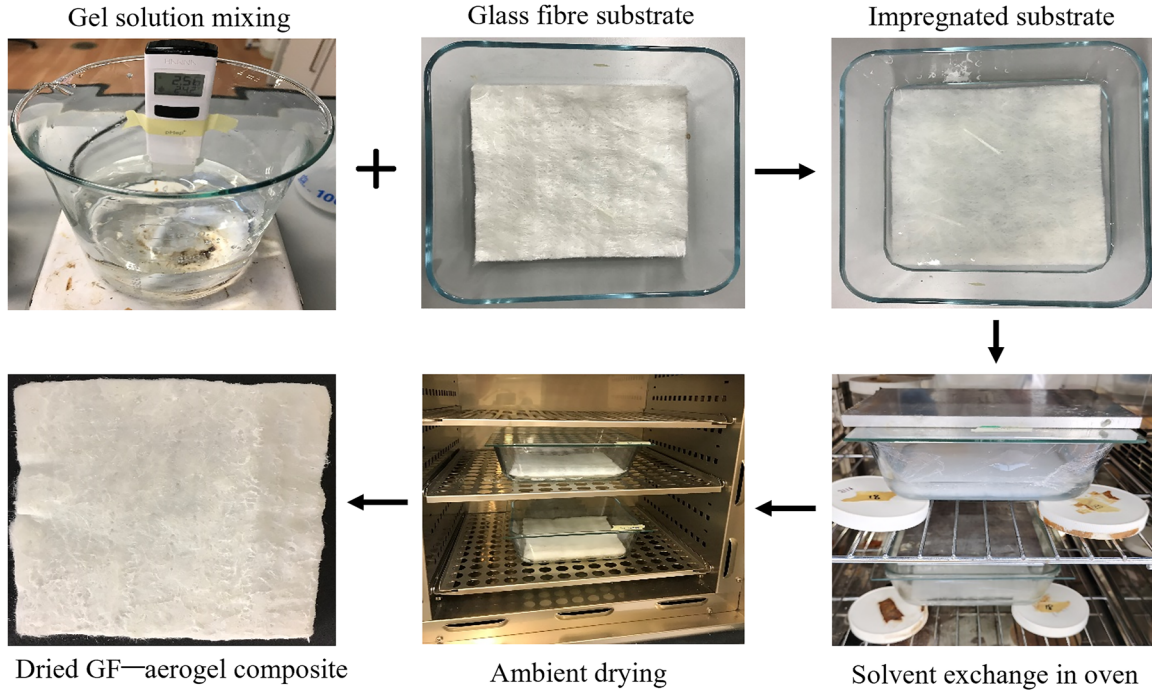


Figure 2: Fabrication process of GF-aerogel composites.

2.3 Sample characterisation

2.3.1 Density and porosity

The bulk density of the aerogel composites was calculated using the measured volume of the samples by ruler and their mass by an electronic balance.

The true density (density of fibre itself without voids in the mat) of the GF mat and PET blanket was measured using a density determination kit. The density determination was performed using Archimedes' principle. This principle states that every solid body immersed in a fluid apparently loses weight by an amount equal to that of the fluid it displaces. The density of the solid can be calculated as follows:²¹

$$\rho = \frac{w_a}{w_a - w_l} (\rho_l - \rho_a) + \rho_a \quad (1)$$

where ρ is the density of the sample, w_a is the weight of the sample in air in g, w_l is the weight of the sample in the liquid (deionised water in this case) in g, ρ_l is the density of the water at measured temperature ($0.99802 \text{ g cm}^{-3}$ at 21°C), ρ_a is the density of air (0.0012 g cm^{-3}).²¹

An average of eight measurements was conducted with errors showing a 95% confidence limit.

The porosity of the aerogel and aerogel composites were calculated as follows:

$$\varphi = \left(1 - \frac{\rho_a}{\rho_s}\right) \times 100\% \quad (2)$$

$$\varphi = \frac{\frac{1}{\rho_a} - \frac{1}{\rho_s} - \frac{1}{\rho_f}}{\frac{1}{\rho_a}} \times 100\% \quad (3)$$

where φ is the porosity, ρ_a is the bulk density of aerogel composites, ρ_s is the skeleton density of the silica aerogel, generally = 2.2 g cm^{-3} ,²² and ρ_f is the true density of fibre measured and calculated using Equation (1).

2.3.2 SEM imaging

The morphology of aerogel composites was investigated by scanning electron microscope (SEM, HITACHI S-3700N) with 5 kV voltage. The samples were gold-coated using an AGAR sputter coater before analysing.

2.3.3 Gas adsorption

Gas adsorption measurements were conducted using a Micromeritics ASAP2420 Surface Area and Porosity Analyser. Surface area, pore volume and average pore size were determined via analysis of the cryogenic nitrogen adsorption/desorption isotherm. Approximately 0.1 g of sample was subject to a degas cycle of 30 min at 50°C , followed by 120 min at 110°C , at a pressure of 10 mHg. This process

removed any residual solvent or surface contaminants from the samples. Degassed samples subsequently underwent a 40-point adsorption cycle between the relative pressures (sample pressure/saturation vapour pressure) of 0.01 and 1, followed by a 30-point desorption cycle between the relative pressures of 1 and 0.1. Sample temperature was maintained at a constant value of $-196\text{ }^{\circ}\text{C}$ throughout the experiment using a liquid nitrogen bath.

2.3.4 Hydrophobicity

Contact angle measurements were obtained using a Kruss DSA30 (Hamburg, Germany) and HPLC grade water (Merck, Switzerland), according to ASTM D5946. The data were analysed in Advance software (Kruss, Germany) using manual fitting of a baseline and shape of the water drops. An average contact angle was calculated based on seven measurements of each sample.

2.3.5 FT-IR analysis

The chemical bonding state of the aerogel was determined via Fourier transform infrared analysis (Agilent Technologies 4100 Exo Scan). The spectral range was set from $4,000$ to 650 cm^{-1} as there is considerable spectral noise outside this range. A diamond ATR (attenuated total internal reflectance) was used as the diffuse reflectance interface. The analysis involved the application of pressure to the samples with a clamp to allow full contact with the diamond ATR crystal. A minimum of 10 specimens was tested, and the raw data generated were analysed using OriginLab.

2.3.6 Thermal gravimetric analysis

Thermal stability, which refers to the temperature up to which the aerogel composite retains its hydrophobicity, was tested by thermal gravimetric analysis (TGA, TA Instruments Q50), according to ASTM E2550. The samples were heat-treated in the air from $20\text{ }^{\circ}\text{C}$ up to $800\text{ }^{\circ}\text{C}$ with a rate of 10 K min^{-1} .

2.3.7 Thermal conductivity

A Netzsch Heat Flow Meter 436 with a thickness gauge was used to measure the thermal conductivity and thickness of aerogel composites accurately, according to ASTM C518-17. The specimens were prepared with a size of $18\text{ cm} \times 18\text{ cm}$. Standard testing was conducted with a compressive load of 13.8 kPa (2 psi) and a mean temperature of $20\text{ }^{\circ}\text{C}$, with a temperature difference between the hot and cold plates of $20\text{ }^{\circ}\text{C}$.

2.3.8 Compression and bending test

The mechanical performance of aerogel composites was evaluated by compression and three-point bending using a 50 kN mechanical tester (Instron 5969). The constant loading rate for the compression test was 0.5 mm min^{-1} , according to ASTM C165, and the specimen's size for compression was $50 \times 50 \times 10\text{ mm}$. The sample dimensions for three-point bending were $100 \times 50 \times 10\text{ mm}$. The support span was set to 60 mm , according to ASTM D790. The sample's flexural stress, flexural strain and flexural modulus of elasticity can be calculated as follows:

$$\sigma_f = \frac{3PL}{2wt^2} \quad (4)$$

$$\varepsilon_f = \frac{6Dt}{L^2} \quad (5)$$

$$E_f = \frac{\sigma_{f_2} - \sigma_{f_1}}{\varepsilon_{f_2} - \varepsilon_{f_1}} \quad (6)$$

where σ_f is the flexural stress in MPa, ε_f is the flexural strain in the outer surface, E_f is the flexural modulus of elasticity in MPa, P is the applied load in N, L is the support span, setting as 60 mm , D is the maximum deflection of the sample centre in mm, W and t are the width and thickness of the specimen in mm, respectively.

3 Results and discussion

3.1 Morphologies and physical properties of aerogel composites

To investigate the influence of ageing temperature on the pore structure of the silica aerogels, the ageing and solvent exchange process of silica gel was conducted at both ambient temperature ($23\text{ }^{\circ}\text{C}$) and $45\text{ }^{\circ}\text{C}$. The ageing process was conducted in EtOH for 24 h, and EtOH was replaced by n-Hexane twice in 32 h for both cases. The physical properties of both samples are summarised in Table 1. It is found that aerogel aged and solvent-exchanged at higher temperatures has a lower apparent density, higher specific surface area and pore volume, and finer average pore diameter. This may be because solvent exchange at a higher temperature increases the solvent diffusivity according to the theory of diffusion in gel, resulting in a higher coarsening of the gel network.²³ This promotes the dissolution and reprecipitation of the silica gel. The further hydrolysis and condensation of unhydrolysed groups and the esterification of silanols occur as well.²⁴

Table 1: Physical properties of the aerogel and aerogel composites.

Sample	Bulk density (g cm^{-3}) ^a	Porosity (%)	BET surface area ($\text{m}^2 \text{g}^{-1}$)	Pore volume ($\text{cm}^3 \text{g}^{-1}$)	Pore size (nm)
Aerogel @23 °C ^b	0.198 ± 0.008	91.0	461 ± 6.8	1.43	13.3
Aerogel @45 °C ^b	0.184 ± 0.018	91.6	726 ± 3.5	2.78	12.1
PET-aerogel	0.10 ± 0.001	87.0	195 ± 5.8	0.66	10.2

^aBulk density of PET fibre mat and glass fibre mat were measured to be 71 g cm^{-3} and 110 g cm^{-3} using density kit, respectively; for reference, the density of commercial Spaceloft aerogel blankets with glass fibres was measured to be 150 g cm^{-3} ; ^bAerogel at 23 °C and 45 °C refer to ageing and solvent exchanging process conducted at room and 45 °C; ^cMeasured at 13.8 kPa @20 °C.

Table 1 summarises the physical properties of the aerogel and aerogel composites. The bulk density of the GF mat and PET blanket is calculated as 0.12 g cm^{-3} and 0.07 g cm^{-3} , while the bulk density of the GF-aerogel and PET-aerogel composites increase slightly to 0.17 g cm^{-3} and 0.10 g cm^{-3} , respectively, according to ASTM C167. This is because the voids in the fibre mat are occupied by aerogel. The true density of the PET and GF fibres was determined based on the measurement described in Section 2.3.1 and calculated using Equation (1). The true density of the GF and PET fibre is $2.56 \pm 0.08 \text{ g cm}^{-3}$ and $1.37 \pm 0.04 \text{ g cm}^{-3}$, respectively. The porosity of the composites was calculated based on Equation (3) using these measured values. The specific surface area was obtained by the Brunauer–Emmett–Teller (BET) model, and the mean pore diameter was calculated by the Barrett–Joyner–Halenda (BJH) method. However, these can

only be used to obtain the surface area and pore volume for a sample pore size less than 100 nm (mainly aerogel). Since the adsorption capacities were measured according to the mass of the sample (per gram), the composites have less pure silica aerogel compared to the neat silica aerogel with the same weight.²⁵ Thus, the BET surface area and pore volume of the aerogel composites are much lower compared to the neat silica aerogel. The pore volume was calculated based on the quantity of adsorbed gas at $P/P_0 = 0.99$ and the density of liquid nitrogen (0.8081 g cm^{-3}). Figure 3 presents photos and microstructures of silica aerogel (a, b), PET-aerogel (c, d), GF-aerogel (e, f), and commercial aerogel blanket with glass fibres (Spaceloft®) (g, h), respectively. Figure 3b (aerogel) shows a highly porous and homogeneous nanostructure. It can be seen from Figure 3d (PET) and f (GF) that the silica aerogel matrix adheres to the PET and glass fibre tightly, and

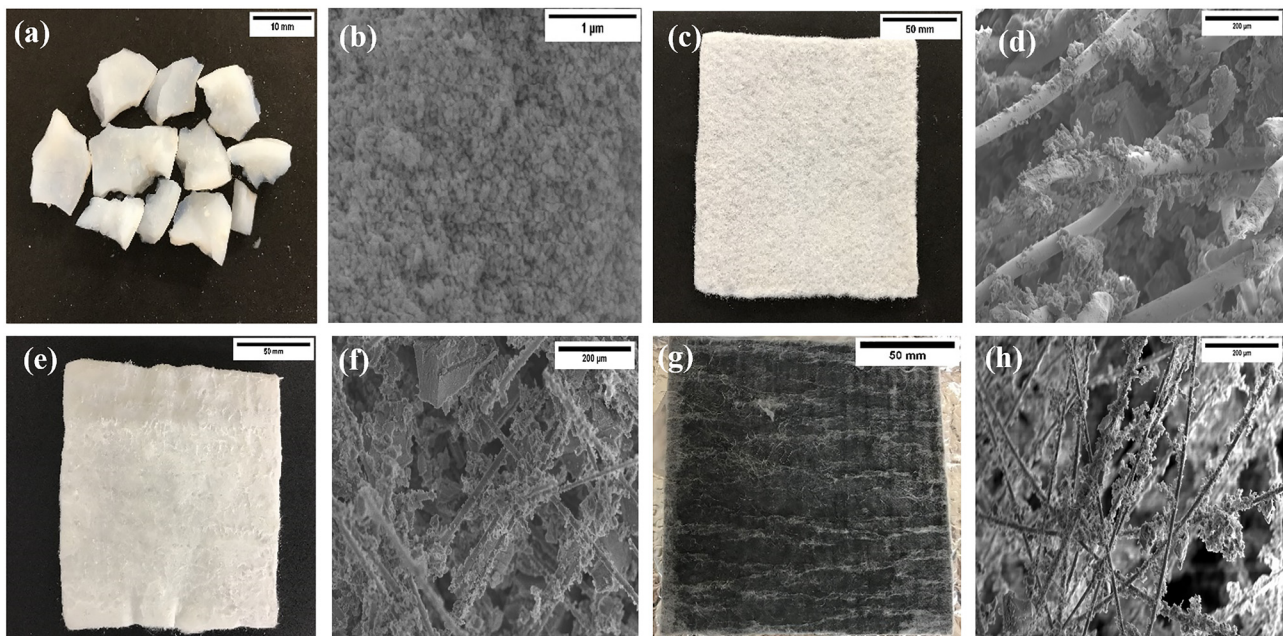


Figure 3: Photos and microstructures of (a, b) silica aerogel granules, (c, d) PET-aerogel, (e, f) GF-aerogel, and (g, h) commercial Aspen spaceloft® blanket with glass fibres, respectively.

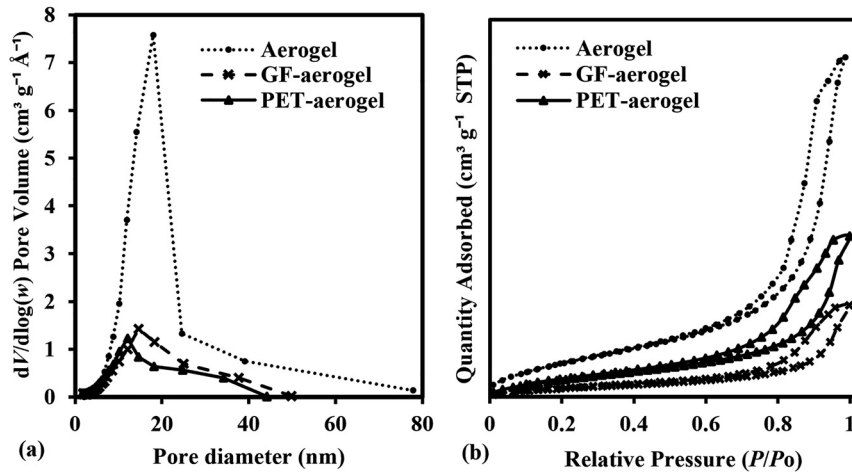


Figure 4: Silica aerogel, GF-aerogel, and PET-aerogel composites: (a) Pore size distribution (PSD), and (b) N_2 adsorption-desorption isotherms.

the microstructure of the commercial aerogel blankets shown in Figure 3h (Spaceloft with glass fibres) is well-replicated in this work (Figure 3f (GF)). Additionally, aerogels also fill in the space between fibres, and such structure could suppress the heat transfer across the composites. This will be discussed in Section 3.3.1.

The pore size distribution (PSD) of the aerogel composites is shown in Figure 4a. It can be seen that the silica aerogel exhibits meso- and macro-pore size region (2–40 nm) and centred at 18 nm, corresponding BJH mean pore diameter of 12.1 nm, as shown in Table 1. Both PET-aerogel and GF-aerogel composites have a narrower pore size distribution, with a mean pore diameter of 10.2 nm and 12.2 nm, respectively. Figure 4b shows the N_2 adsorption-desorption isotherm of the aerogel, GF-aerogel and PET-aerogel composites. It presents a type IV(a) isotherm with a H3 hysteresis loop at $P/P_0 > 0.6$, revealing the mesoporous characteristics of the aerogel.²⁶ The sharp increase of isotherms in the high relative pressure region ($P/P_0 = 0.95$ – 1.0) is due to the liquid condensation, suggesting the presence of macropores.⁶ The fibre-reinforced aerogel composites retain the aerogel nature in terms of the microstructure. The pore sizes are much smaller than the mean free path of air (70 nm) in the atmosphere, which could reduce the heat transfer via the gaseous phase. Thus, the thermal insulation performance of the aerogel composites might be improved.⁶

3.2 Hydrophobicity and FTIR spectra of aerogel composites

Figure 5a–f shows photos and microscopic images of a water droplet on the surface of neat silica aerogel, PET-aerogel and GF-aerogel composites, respectively. The average water contact angle is $129^\circ \pm 13^\circ$, $138^\circ \pm 14^\circ$ and $121^\circ \pm 9^\circ$,

respectively. This excellent water-repellent behaviour stemmed from the treatment of the specimens with TMCS, where the stable methyl groups are responsible for the superior hydrophobicity of the silica components.¹³

Figure 6 shows the FTIR spectra of silica aerogel, glass fibre and GF-aerogel composites. The band at $1,060 \text{ cm}^{-1}$ is caused by the symmetric stretching vibrations of Si–O–Si bonds,²⁷ and the peak at 900 cm^{-1} shows the characteristics of stretching bands of the Si–OH for E-glass fibre. The TMCS-hydrophobisation aerogel and aerogel composites show strong absorption peaks at about 850 cm^{-1} , $1,260 \text{ cm}^{-1}$ and $2,980 \text{ cm}^{-1}$, corresponding to Si– CH_3 groups and $-\text{CH}_3$ groups.^{2,6} The presence of these absorption peaks confirms the attachment of $-\text{Si}-\text{CH}_3$ groups from the TMCS to the silica aerogel surface, indicating that the surface modification process was successful. Moreover, the bonds at $\sim 3,450 \text{ cm}^{-1}$ and $\sim 1,650 \text{ cm}^{-1}$ representing $-\text{OH}$ groups disappear after surface modification.

Figure 7 shows the FTIR spectra of silica aerogel and aerogel after heat treatment (800°C). It can be seen that the strong absorption peaks at about 850 cm^{-1} , $1,260 \text{ cm}^{-1}$ and $2,980 \text{ cm}^{-1}$, corresponding to Si– CH_3 groups and $-\text{CH}_3$ groups, disappeared after thermal treatment at high temperatures due to pyrolysis. The heat-treated aerogel becomes hydrophilic; thus, it will absorb water, which could diminish the thermal insulation performance.

3.3 Thermal properties of aerogel composites

3.3.1 Thermal conductivity of aerogel blankets

Figure 8 shows the measured thermal conductivity of PET blanket, GF mat, PET-aerogel and GF-aerogel composites at

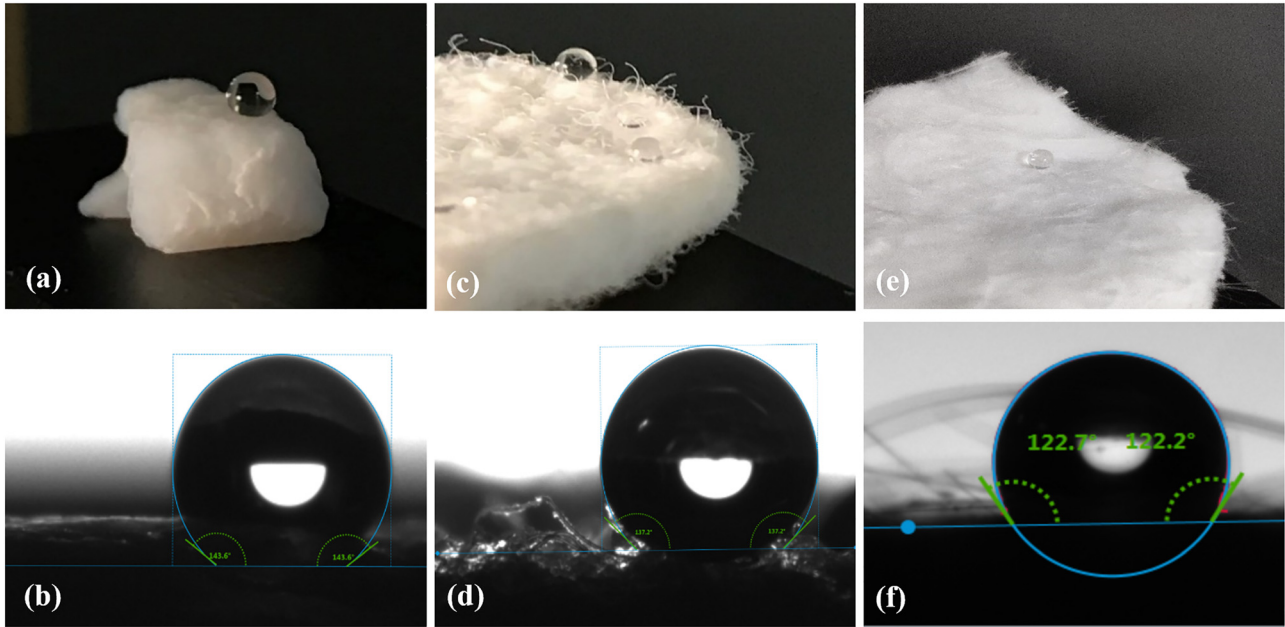


Figure 5: (a), (c), (e) Photos of a water droplet on the surface and (b), (d), (f) microscopic images of water contact angle of neat silica aerogel, PET-aerogel and GF-aerogel composites, respectively.

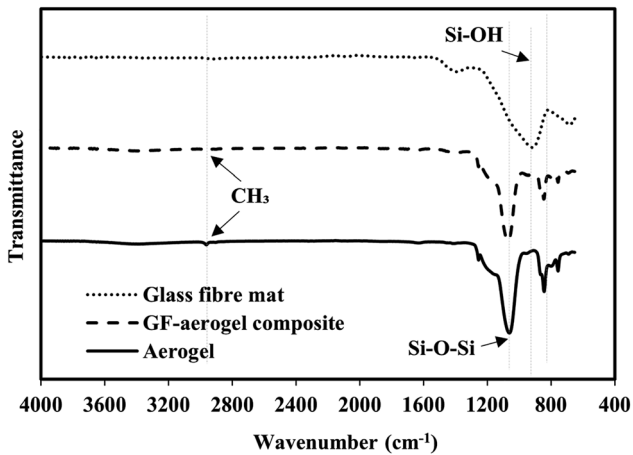


Figure 6: FTIR spectra of glass fibre, silica aerogel, and GF-aerogel composite.

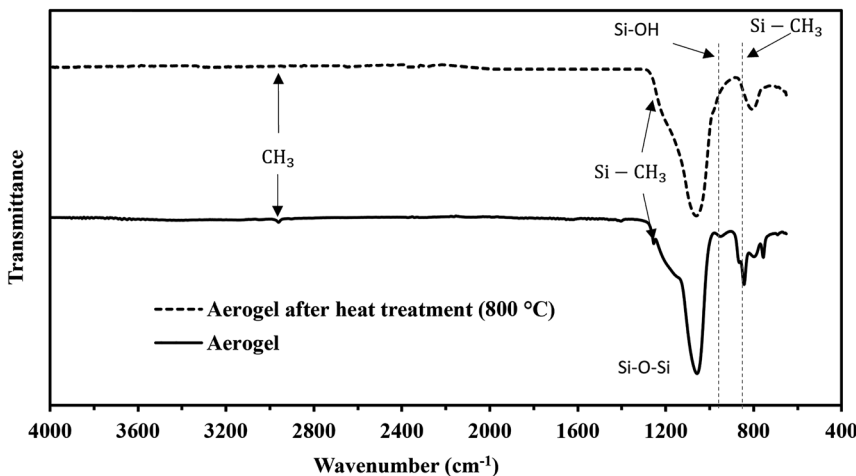


Figure 7: FTIR spectra of silica aerogel and silica aerogel after heat treatment (800 °C).

a mean temperature of 20 °C, with a constant loading pressure of 2 psi. A noticeable improvement in thermal conductivity is achieved when aerogel is introduced into the fibre matrix, especially for GF-aerogel composite, where the thermal conductivity drops from 29.6 mW m⁻¹ K⁻¹ to 18.4 mW m⁻¹ K⁻¹. A slight improvement can be found for PET-aerogel composites (reduced from 27.4 mW m⁻¹ K⁻¹ to 24.3 mW m⁻¹ K⁻¹). This behaviour can be explained through the combination heat transfer mechanism of porous materials, including solid conduction by fibre and aerogel particles, gas conduction inside aerogel pores and voids between fibres, convection in voids between fibres, and radiation.

In porous insulating materials, the total effective heat transfer is dominated by the contribution of the non-convective gas within the hollow spaces or pores.²⁸ The gas conductivity in a porous medium is determined by the

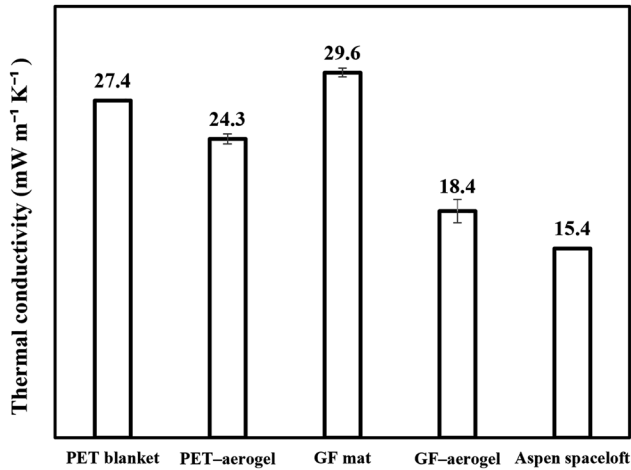


Figure 8: Measured thermal conductivity for PET blanket, PET-aerogel, glass fibre mat, GF-aerogel, and commercial Aspen Spaceloft[®] blanket at a constant pressure load of 2 psi, with a mean temperature of 20 °C.

number of gas molecules as a transfer medium as well as by the number of ‘walls’ on the way from the hot to the cold side.²⁸ It is stated that convection in a porous medium can be neglected if the material’s pores are less than 4 mm.^{29,30} In addition, radiation contributes an approximate 5 % portion of total thermal conductivity at room temperature, and this portion increases as temperature increases.²⁹ A reduction in the insulating material’s gas thermal conductivity is achieved by either reducing the pressure or introducing a nanostructured core material.³¹ By reducing the pressure, the number of gas particles in a given volume of space is reduced; thus, the mean free path between collisions of particles is increased.³¹ When the pore diameter of the material becomes less than the mean free path of gas molecules, such as in aerogels, the molecules will only collide with the pore surface without transferring energy, known as the Knudsen effect.³¹ The heat transfer in the solid grain of aerogel should flow mainly through phonons or localised oscillations.³⁰ As the solid grain sizes of aerogel are in the range of 2–5 nm, the phonon–grain boundaries scattering occupies the main position and lowers the phonon mean free path in aerogel; thus, the solid thermal conductivity is reduced.³⁰

3.3.2 Thermal conductivity of vacuum-sealed aerogel blankets

Figure 9 shows the comparison of thermal conductivity of aerogel composite under ambient and vacuum at a mean temperature of 20 °C, with a constant loading pressure of 2 psi. A noticeable reduction in the thermal conductivity can

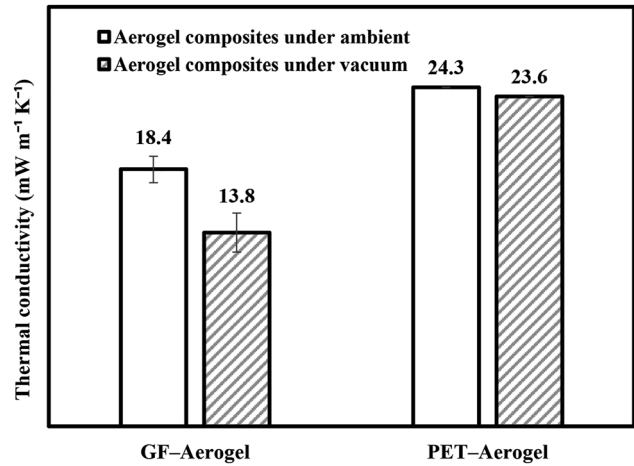


Figure 9: The comparison of thermal conductivity of GF-aerogel and PET-aerogel under ambient and vacuum at a mean temperature of 20 °C, with a constant loading pressure of 2 psi.

be found for the GF-aerogel sample. The thermal conductivity decreases from 18.4 mW m⁻¹ K⁻¹ to 13.8 mW m⁻¹ K⁻¹, with 25 % reduction. As mentioned previously, the heat transfer of fibre-reinforced aerogel composites consists of solid conduction, gaseous conduction and radiation. It was stated that the most effective way of improving the thermal insulation properties of materials is to reduce the gaseous thermal conductivity.³¹ When a vacuum system is introduced, the number of gas particles in a given volume of space is reduced or eliminated; thus, the mean free path between collisions of particles is increased.³¹ When the pore diameter of the material becomes less than the mean free path of gas molecules, the molecules will only collide with the pore surface without transferring energy (Knudsen effect). Therefore, the heat transfer by the gas phase present within the composite is minimised. Thus, a lower thermal conductivity value can be achieved.

Figure 9 also shows that only a 3 % reduction in the thermal conductivity is obtained for the PET-aerogel sample. As mentioned previously, a slight decrease in thermal conductivity is obtained when aerogel is reinforced by a PET blanket (reduced from 27.4 mW m⁻¹ K⁻¹ to 24.3 mW m⁻¹ K⁻¹) under ambient conditions. This may be because the porosity of the GF mat (95.5 %) is slightly higher than the PET blanket (94.9 %), as shown in Table 1. It leads to a higher mass percentage of aerogel in the GF-aerogel composite as more voids can be occupied by aerogel. Thus, the reduction in thermal conductivity of GF-aerogel is higher than that of the PET-aerogel composite. Another possible reason could be related to the vacuum level not being measured well enough.

3.3.3 Thermal conductivity of aerogel composites at various pressure loads

The thermal conductivity of glass fibre-reinforced aerogel composite against various loading pressures is shown in Figure 10. The result shows that lower thermal conductivity is achieved with higher pressure, and there is no sign of level-off with continuing increasing pressure. However, the applied load is limited by the apparatus. The thermal conductivity of GF-aerogel composite can reach as low as $18.6 \text{ mW m}^{-1} \text{ K}^{-1}$ at a pressure of 15 kPa, which is significantly lower than conventional organic foams (i.e. EPS, $35 \text{ mW m}^{-1} \text{ K}^{-1}$). As mentioned previously, gas conductivity is the dominant heat transfer path. Compressing the composite blanket results in a change in its microstructure; thus, the porosity varies with compression. Assuming that the volume of fibres and aerogel particles (solid volume) does not change at each loading step, only the pore volume decreases.³² Based on the mathematical model developed in Hoseini, the porosity of the GF-aerogel composite decreases slightly as the pressure load increases.³² As the composite is compressed, densification likely occurs as a result of a better entanglement of clusters, leading to a decrease in the pore size located between clusters.³² This suppresses gas conduction heat transfer due to fewer collisions between gas molecules and an increasing number of elastic collisions between gas molecules and the pore wall.³³ Thus, the thermal conductivity decreases with increasing pressure load. A similar conclusion was drawn by Lakatos.³⁴ It is worth mentioning that in Lakatos' work, the thermal conductivity of the aerogel composites dropped slightly from $19.5 \text{ mW m}^{-1} \text{ K}^{-1}$ to $18.4 \text{ mW m}^{-1} \text{ K}^{-1}$ as the applied load increased, whereas in this work, the thermal conductivity of

the prepared GF-aerogel decreased from $22.1 \text{ mW m}^{-1} \text{ K}^{-1}$ to $18.6 \text{ mW m}^{-1} \text{ K}^{-1}$. This may be because of a higher thickness change (36.7 %), so as the density (57 %) of the GF-aerogel as the applied load increases from 1 kPa to 15 kPa, compared to Lakatos' work (17 % and 15 %). At lower loads, a considerable amount of voids are present within GF-aerogel, leading to a higher thermal conductivity of the materials; where at higher load (15 kPa), the air content is removed. Thus, an almost same thermal conductivity value compared to Lakatos' work is obtained.

3.3.4 Thermal stability analysis

The TGA curve of synthesised silica aerogel, PET-aerogel and GF-aerogel composites is shown in Figure 11. It is well shown that a decrease in the gravity curve of aerogel is presented at a temperature of approximately 400°C due to the oxidisation of the $-\text{CH}_3$ group. A slight weight loss before 100°C is observed due to the evaporation of the residual solvent and water molecules.² No apparent weight loss can be seen for the glass fibre mat due to its pure inorganic composition. By introducing inorganic glass fibre, the aerogel composite maintained almost 95 % of its weight, where only 5 % of the weight is lost at 800°C . The manufactured glass fibre-reinforced aerogel composite achieves excellent thermal stability at a high temperature. PET-aerogel composite remains thermally stable up to 300°C , which significantly limits their use. Kovacs also investigated the thermal stability of aerogel insulation materials at elevated temperatures, which provided a valuable guide for predicting the lifetime of the used insulating material during their industrial use.³⁵

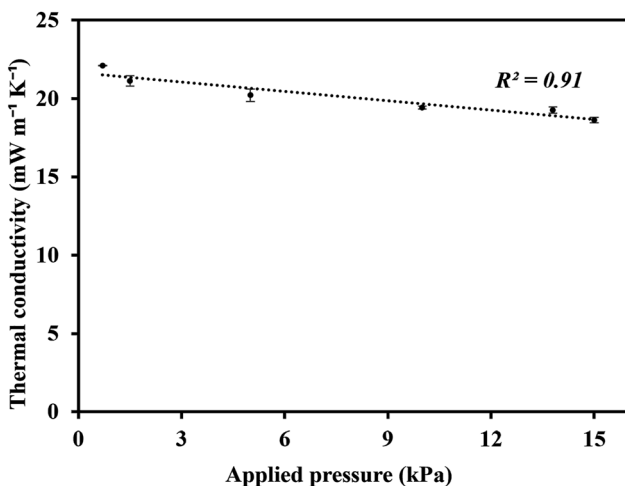


Figure 10: Thermal conductivity of glass fibre reinforced aerogel composite at various loading pressures with a mean temperature of 20°C .

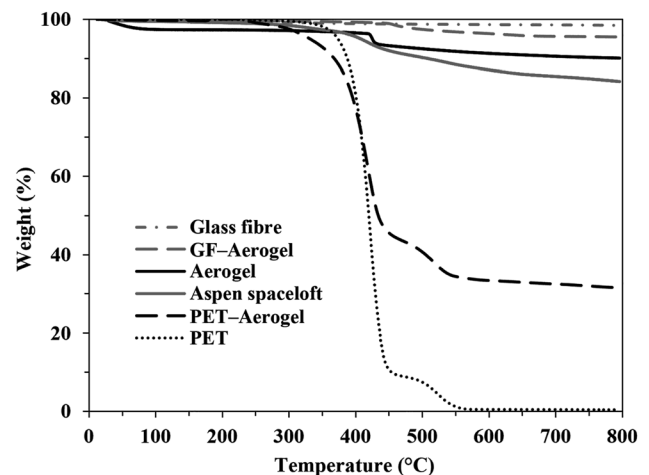


Figure 11: TGA curve of PET blanket, PET-aerogel, GF mat, GF-aerogel composite, and commercial Aspen blanket.

3.4 Mechanical properties of aerogel composites

Figure 12 summarises the compressive strength of neat PET blanket, PET–aerogel composite, glass fibre mat, and GF–aerogel composites. Fibre-reinforced aerogel composites exhibit excellent compressive performance compared to the specimen without aerogel, especially for GF–aerogel composites. A three-fold improvement in compressive strength (4.7 kPa) is achieved at 25 % strain compared to the neat glass fibre mat (1.12 kPa). This can be explained using the stress–strain curve shown in Figure 13. Figure 13 shows the stress–strain curve of GF mat, GF–aerogel, PET blanket, and PET–aerogel composites. In general, the stress–strain

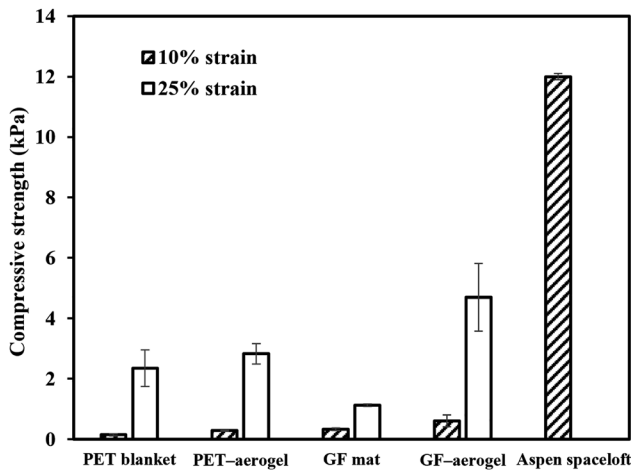


Figure 12: Compressive strength of PET blanket, PET–aerogel composite, glass fibre mat, GF–aerogel composite and commercial Aspen blanket at 10 % and 25 % strain.

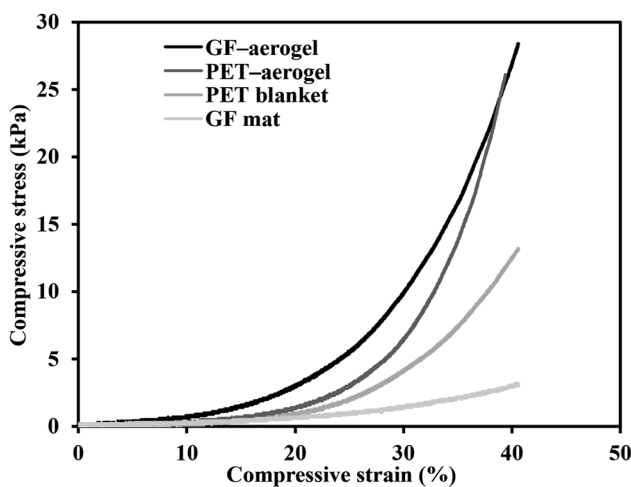


Figure 13: The compressive stress–strain curves of GF–aerogel composite and GF mat.

curve of GF–aerogel and PET–aerogel can be divided into four different stages: the contact stage, the linear stage, the yielding stage, and the densification stage.⁶ At the contact stage, the strain varied from 0 % to 15 % is caused by the uneven surface of the specimens. The stress does not vary significantly at this stage. The strain in the range of 20 %–25 % represents the linear stage, where the slope of the curve remains relatively steady (0.045 ± 0.005 MPa to 0.054 ± 0.005 MPa for GF–aerogel). The nanopores of silica aerogel act as the main load capacity part, while the fibres are only responsible for the structural integrity of the composites.³⁶ The linear stage between the composites and the neat fibre is well distinguished in Figure 13. The strain in the range of 25 %–40 % shows the yielding and densification stage, where the stress increases significantly. At the yield stage, fibres act as the main load capacity part, resulting in a rapid increase in stress. At the densification stage, the significant increase in stress is mainly due to the collapse of aerogel and the gradual densification of the porous structure.³⁶ However, the manufactured aerogel composite is more compressible than the commercial aerogel blanket, and one of the reasons could be that different processes may be adopted to manufacture the GF mat. For example, the fibre mat used in this work is fluffier, resulting in significantly lower resistance to compressive load.

The flexural strength of PET blanket, PE–aerogel, glass fibre mat, and GF–aerogel is summarised in Figure 14. It is evident that fibre-reinforced aerogel composite shows excellent flexural performance compared to that of the specimen without aerogel, especially for glass fibre-reinforced aerogel composite. Nearly three-fold improvement in flexural strength is achieved at 25 % strain compared to the neat GF

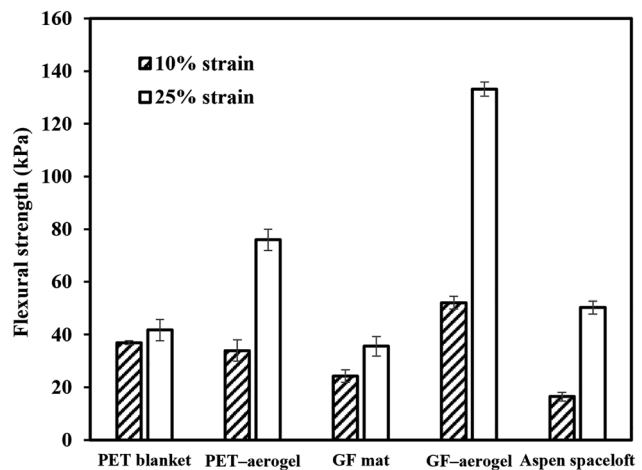


Figure 14: Flexural strength of PET blanket, PET–aerogel composite, glass fibre mat, GF–aerogel composite and commercial Aspen blanket at 10 % and 25 % strain.

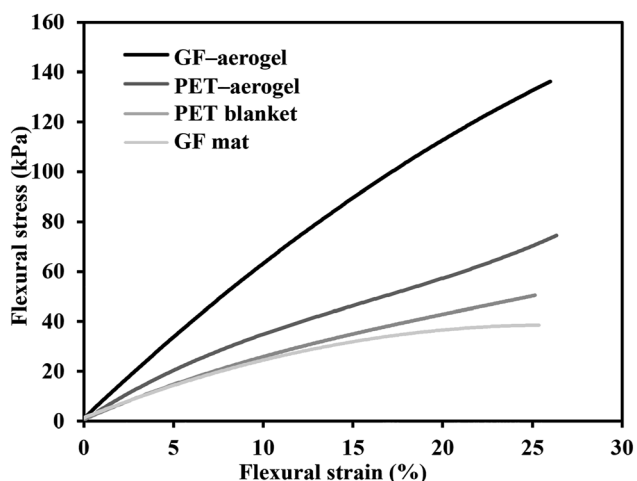


Figure 15: The flexural stress–strain curves of GF–aerogel composite and GF mat.

mat. This is well indicated in the stress–strain curve shown in Figure 15. The strain from 0 % to 10 % in Figure 15 indicates a linear stage where the slope of the curve remains relatively steady (0.5 ± 0.1 MPa to 0.6 ± 0.1 MPa for GF–aerogel). The strain from 10 % to 25 % shows a non-linear stage with a declining slope, meaning that the resistance to deformation tends to decrease. This is due to the layers split of the composites as the top side surface is in compression where the bottom side surface is in tension.

4 Conclusions

In this paper, glass fibre mats were embedded in silica sol to form fibre-reinforced aerogel composites. The fabrication process, including the ageing temperature and drying process, was optimised to improve the physical, thermal and mechanical properties of the aerogel composite. The prepared aerogel composite was then vacuum sealed to prevent dustiness during handling, and its influence on thermal conductivity was investigated.

It was experimentally demonstrated that there was a minimum solvent-to-gel ratio (2:1) to fabricate aerogel successfully. This finding provides guidance for fabricating aerogel with a minimum amount of solvent if the manufacturing cost is considered. The aerogel aged and solvent exchanged at a higher temperature (45°C) led to a lower apparent density, higher specific surface area and pore volume, and finer average pore diameter. The GF–aerogel composites obtained from the optimised process showed excellent thermal conductivity ($18.4\text{ mW m}^{-1}\text{ K}^{-1}$ at a pressure load of 2 psi). It is worth mentioning that vacuum sealing of the aerogel composites not only prevents dustiness during handling but also

improves the thermal performance. The thermal conductivity could be further reduced to $13.8\text{ mW m}^{-1}\text{ K}^{-1}$ by vacuum sealing the GF–aerogel composite. The influence of the pressure load on the thermal conductivity of the GF–aerogel composites was also investigated. The result showed that lower thermal conductivity was achieved with higher pressure, and there was no sign of level-off if the load pressure continued to increase. This might be attributed to the microstructure change under compression. The GF–aerogel composites also possessed excellent thermal stability. The aerogel composites maintained almost 95 % of their weight, where only 5 % of the weight was lost at 800°C . The compression and bending tests proved that the aerogel composites could endure considerable compressive and flexural strain without structural destruction. These outstanding characteristics indicate that GF–aerogel composites have great potential in the thermal insulation field, especially for a moderate temperature environment (i.e., less than 800°C).

References

1. Linhares, T.; Pessoa de Amorim, M. T.; Durães, L. *J. Mater. Chem. A* **2019**, 7 (40), 22768–22802. <https://doi.org/10.1039/c9ta04811a>.
2. He, S.; Huang, D.; Bi, H.; Li, Z.; Yang, H.; Cheng, X. *J. Non-Cryst. Solids* **2015**, 410, 58–64. <https://doi.org/10.1016/j.jnoncrysol.2014.12.011>.
3. IUPAC *Compendium of Chemical Terminology (Gold Book)*; Blackwell Publishing: Oxford, 2014.
4. Neugebauer, A.; Chen, K.; Tang, A.; Allgeier, A.; Glicksman, L. R.; Gibson, L. J. *Energy Buildings* **2014**, 79, 47–57. <https://doi.org/10.1016/j.enbuild.2014.04.025>.
5. Li, C.; Zhang, G.; Lin, L.; Wu, T.; Brunner, S.; Galmarini, S.; Bi, J.; Malfait, W. J.; Zhao, S.; Ostrikov, K. *Int. Mater. Rev.* **2023**, 68 (7), 862–900. <https://doi.org/10.1080/09506608.2023.2167547>.
6. Shafi, S.; Navik, R.; Ding, X.; Zhao, Y. *J. Non-Cryst. Solids* **2019**, 503–504, 78–83. <https://doi.org/10.1016/j.jnoncrysol.2018.09.029>.
7. Huang, Y.; He, S.; Chen, G.; Dai, H.; Yuan, B.; Chen, X.; Yang, X. *J. Non-Cryst. Solids* **2019**, 505, 286–291. <https://doi.org/10.1016/j.jnoncrysol.2018.11.003>.
8. Lyu, S.; Yang, X.; Shi, D.; Qi, H.; Jing, X.; Li, S. *Sci. China Technol. Sci.* **2017**, 60 (11), 1681–1691. <https://doi.org/10.1007/s11431-016-9092-2>.
9. Ślosarczyk, A. *J. Sol-Gel Sci. Technol.* **2017**, 84 (1), 16–22. <https://doi.org/10.1007/s10971-017-4470-4>.
10. Jiang, Y.; Feng, J.; Feng, J.; Shi, C. High-Temperature Mechanical Properties of Silica Aerogel Composites Reinforced by Mullite Fibers. In: *Advances in High Temperature Ceramic Matrix Composites and Materials for Sustainable Development; Ceramic Transactions*, Vol. CCLXIII; John Wiley & Sons, Inc., 2017; pp. 333–339.
11. Chakraborty, S.; Pisal, A. A.; Kothari, V. K.; Venkateswara Rao, A. *Adv. Mater. Sci. Eng.* **2016**, 2016, 1–8. <https://doi.org/10.1155/2016/2495623>.
12. Li, Z.; Cheng, X.; He, S.; Shi, X.; Gong, L.; Zhang, H. *Composites, Part A* **2016**, 84, 316–325. <https://doi.org/10.1016/j.compositesa.2016.02.014>.
13. Salomo, S.; Nguyen, T. X.; Le, D. K.; Zhang, X.; Phan-Thien, N.; Duong, H. M. *Colloids Surf., A* **2018**, 556, 37–42. <https://doi.org/10.1016/j.colsurfa.2018.08.015>.
14. Talebi, Z.; Soltani, P.; Habibi, N.; Latifi, F. *Constr. Build. Mater.* **2019**, 220, 76–89. <https://doi.org/10.1016/j.conbuildmat.2019.06.031>.

15. Zhai, J.; Yang, D.; Han, J. *J. Build. Mater. Technol. Appl.* **2018**, *5*, 5–10. <https://doi.org/10.13923/j.cnki.cn14-1291/tu.2018.05.002>.
16. Liang, Y.; Wu, H.; Huang, G.; Yang, J.; Wang, H. *Energy Buildings* **2017**, *154*, 606–617. <https://doi.org/10.1016/j.enbuild.2017.08.085>.
17. Venkataraman, M.; Mishra, R.; Kotresh, T. M.; Militky, J.; Jamshaid, H. *Text. Prog.* **2016**, *48* (2), 55–118. <https://doi.org/10.1080/00405167.2016.1179477>.
18. Adl-Zarrabi, B.; Johansson, P., Eds. Long-Term Performance of Super-insulating-materials in Building Components & Systems. In *Report of Subtask III: Practical Applications Retrofitting at the Building Scale Field scale*; International Energy Agency, 2015.
19. Heinemann, U., Ed. Long-Term Performance of Super-insulating Materials in Building Components and Systems. In *Report of Subtask I: State of the Art and Case Studies*; International Energy Agency, 2020.
20. Wang, K. Novel Development of Eco-Friendly Porous Thermal Insulation Materials and the Application. In *Mechanical and Aerospace Engineering*; Glasgow, UK: University of Strathclyde, 2022.
21. Ag, M.-T. *Operating Instructions of Density Kit*; Greifensee, Switzerland: Mettler-Toledo AG.
22. Venkateswara Rao, A.; Sakhare, H. M.; Tamhankar, A. K.; Shinde, M. L.; Gadave, D. B.; Wagh, P. B. *Mater. Chem. Phys.* **1999**, *60* (3), 268–273. [https://doi.org/10.1016/S0254-0584\(99\)00089-9](https://doi.org/10.1016/S0254-0584(99)00089-9).
23. Jiang, Y.; Feng, J.; Feng, J. *J. Sol-Gel Sci. Technol.* **2017**, *83* (1), 64–71. <https://doi.org/10.1007/s10971-017-4383-2>.
24. Omranpour, H.; Motahari, S. *J. Non-Cryst. Solids* **2013**, *379*, 7–11. <https://doi.org/10.1016/j.jnoncrysol.2013.07.025>.
25. Zhang, Z.; Jun, S.; Ni, X.; Wu, G.; Zhou, B.; Yang, M.; Gu, X.; Qian, M.; Wu, Y. Macromolecular Science, Part A. *Pure Appl. Chem.* **2007**, *43* (11), 1663–1670. <https://doi.org/10.1080/10601320600934792>.
26. Thommes, M.; Kaneko, K.; Neimark, A. V.; Olivier, J. P.; Rodriguez-Reinoso, F.; Rouquerol, J.; Sing, K. S. W. *Pure Appl. Chem.* **2015**, *87* (9–10), 1051–1069. <https://doi.org/10.1515/pac-2014-1117>.
27. Moreno-Maldonado, V.; Acosta-Torres, L. S.; Barceló-Santana, F. H.; Vanegas-Lancón, R. D.; Plata-Rodríguez, M. E.; Castaño, V. M. *J. Appl. Polym. Sci.* **2015**, *132* (2). <https://doi.org/10.1002/app.41510>.
28. Simmler, H.; Brunner, S.; Heinemann, U.; Schwab, H.; Kumaran, K.; Mukhopadhyaya, P.; Quenard, D.; Sallee, H.; Noller, K.; Kuecukpinar-Niarchos, E.; Stramm, C.; Tenpierik, M.; Cauberg, H.; Erb, M. *Vacuum Insulation Panels – Study on VIP-Components and Panels for Service Life Prediction of VIP in Building Applications (Subtask A)*; Berne, Switzerland: Swiss Federal Office of Energy, 2005.
29. Hoseini, A.; McCague, C.; Andisheh-Tadbir, M.; Bahrami, M. *Int. J. Heat Mass Transfer* **2016**, *93*, 1124–1131. <https://doi.org/10.1016/j.ijheatmasstransfer.2015.11.030>.
30. Wei, G.; Liu, Y.; Zhang, X.; Yu, F.; Du, X. *Int. J. Heat Mass Transfer* **2011**, *54* (11), 2355–2366. <https://doi.org/10.1016/j.ijheatmasstransfer.2011.02.026>.
31. Shatav, M.; Elmer, T.; Tetlow, D.; Riffat, S. The State of the Art Superinsulation Construction Materials under the UK's Domestic Energy Building. In *14th International Conference on Sustainable Energy Technologies*; Nottingham, UK, 2015.
32. Hoseini, A.; Malekian, A.; Bahrami, M. *Energy Buildings* **2016**, *130*, 228–237. <https://doi.org/10.1016/j.enbuild.2016.08.053>.
33. Johansson, P. *Building Retrofit using Vacuum Insulation Panels*; Department of Civil and Environmental Engineering, Chalmers University of Technology: Sweden, 2014.
34. Lakatos, Á.; Csík, A.; Csarnovics, I. *Case Stud. Therm. Eng.* **2021**, *25*. <https://doi.org/10.1016/j.csite.2021.100966>.
35. Kovács, Z.; Csík, A.; Lakatos, Á. *Therm. Sci. Eng. Prog.* **2023**, *42*. <https://doi.org/10.1016/j.tsep.2023.101906>.
36. Zhou, T.; Cheng, X.; Pan, Y.; Li, C.; Gong, L.; Zhang, H. *Appl. Surf. Sci.* **2018**, *437*, 321–328. <https://doi.org/10.1016/j.apsusc.2017.12.146>.